

3D OPTICAL FLOW FROM DOPPLER AND WINDPROFILER RADAR DATA

Yong Zhang, John L. Barron and Robert E. Mercer

Dept. of Computer Science, The University of Western Ontario, London, N6A 5B7, Ontario, Canada

Keywords: 3D Doppler radial velocity, 3D Windprofiler velocity, 3D Least squares optical flow, 3D Regularized optical flow, 3D Full velocity field.

Abstract: We describe an application that combines velocity data from a Windprofiler radar and a NEXRADII Doppler radar to compute 3D optical flow of moving severe weather. Windprofiler data improves the recovery of the velocity component in the upwards direction in the optical flow, where Windprofiler data is believed to be more accurate. We demonstrate this quantitatively using synthetic radar data and qualitatively using real radar data from Detroit NCDC Doppler and Harrow Windprofiler radars.

1 INTRODUCTION

Doppler radar is an important meteorological observation tool. To gain knowledge of how storms move over time, much research has been devoted to retrieving 3D full velocity from the observed radial velocity (for example, Lhermitte and Atlas (Lhermitte and Atlas, 1961), Easterbrook (Easterbrook, 1975) and Waldteufel and Corbin (Waldteufel and Corbin, 1979)). Rather than using the traditional methods provided by meteorologists, our research group is solving this problem using the 3D Optical Flow framework (Barron et al., 2005), which is a technology widely applied in Computer Vision. In this paper, we “refine” 3D Doppler optical flow by integrating Windprofiler data into the calculation. We illustrate this refinement using data from the Detroit NCDC Doppler and the Harrow Windprofiler radars.

Doppler data consist of a number of (15-16) cones of data where each cone wall has a different but constant angle (0° to about 20°) with the flat ground. Each cone is constructed from 360 equally spaced rays and data is sampled at equal distances along each ray. We use a right-handed coordinate system where the x and y axes describe a plane and the z axis the height of the data. Optical flow is a 3D vector field, (U, V, W) , and is the 3D motion of water precipitation over time. At lower elevation angles in the data, we note that the W velocity component is almost orthogonal to the radial velocities: in the presence of even small amounts of noise, radial velocity contains little recoverable W information.

2 COMPUTING OPTICAL FLOW

We have extended Horn and Schunck’s 2D regularization method to 3D (Horn and Schunck, 1981). Now a number of constraint terms on 3D velocity are minimized (regularized) over the 3D domain.

The first term we use is the 3D **Radial Velocity Constraint**, which requires that the full velocity projected in the radial direction be the radial velocity:

$$\vec{V} \cdot \hat{r} = V_r, \quad (1)$$

where $\vec{V} = (U, V, W)$ is the local 3D velocity (which we want to compute), \hat{r} is the local unit radial velocity direction (known precisely from the radar setup) and V_r is the measured local radial velocity magnitude.

The second constraint is a 3D Horn and Schunck-like **Velocity Smoothness Constraint**, which requires that velocity vary smoothly everywhere by keeping velocity component derivatives in the 3 dimensions as small as possible.

Thirdly, the **Least Squares Velocity Consistency Constraint** is based on an extension of the 2D Lucas and Kanade least squares optical flow algorithm (Lucas and Kanade, 1981) into 3D. This constraint assumes that 3D velocity is locally constant in local neighbourhoods but that the local radial velocity varies in these $N \times N \times N$ neighbourhoods. A least squares calculation is then performed for each neighbourhood:

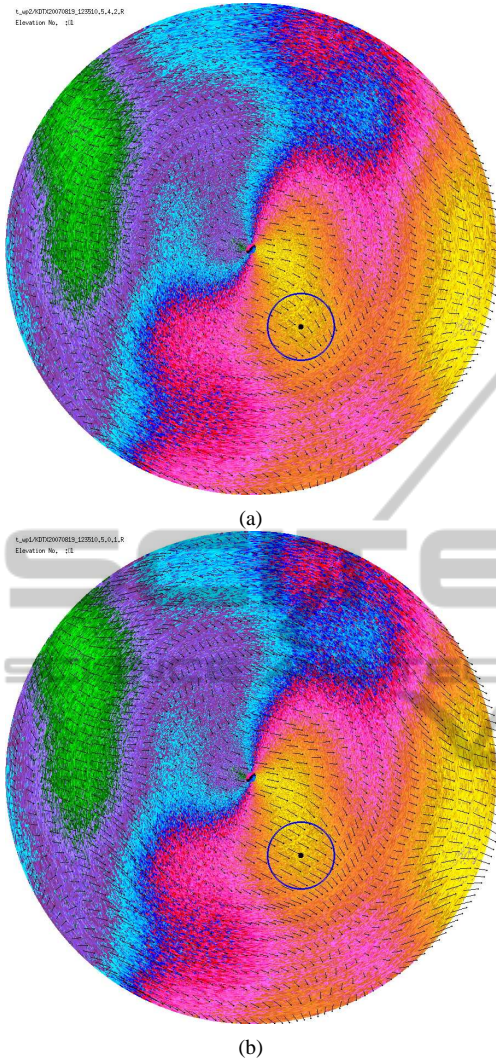


Figure 1: The retrieved synthetic velocity at variation level $K = 5$: (a) the unrefined UV optical flow and (b) the refined UV optical flow.

$$\underbrace{\begin{bmatrix} r_{X_1} & r_{Y_1} & r_{Z_1} \\ r_{X_2} & r_{Y_2} & r_{Z_2} \\ \dots & \dots & \dots \\ r_{X_N} & r_{Y_N} & r_{Z_N} \end{bmatrix}}_A \begin{bmatrix} U_{I_s} \\ V_{I_s} \\ W_{I_s} \end{bmatrix} = \begin{bmatrix} V_{r_1} \\ V_{r_2} \\ \dots \\ V_{r_N} \end{bmatrix}. \quad (2)$$

If matrix $A^T A$ can be reliably inverted the least squares velocity $\vec{V}_{I_s} = (U_{I_s}, V_{I_s}, W_{I_s})$ can be recovered. This allows us to use a constraint which requires computed velocities to be consistent with local least squares velocities.

And lastly, the **Windprofiler Velocity Consistency Constraint**, incorporates the Windprofiler velocity estimates, \vec{V}_{wpr} , into the regularization, again by requiring local values of \vec{V}_{wpr} and \vec{V} be consistent.

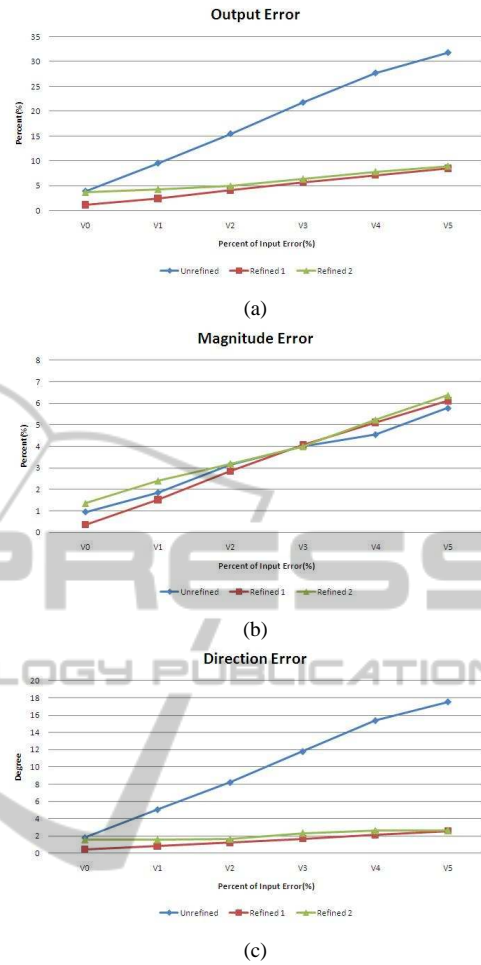


Figure 2: Error results of the synthetic data for all K values: (a) the average output error, (b) the average magnitude error and (c) the average direction error. Refined (red) lines represent 0% Windprofiler error while Refine2 (green) lines represent 10% Windprofiler error.

The regularization functional is the sum of these constraints:

$$\int \int \int \left(\underbrace{(\vec{V} \cdot \hat{r} - V_r)^2}_{\text{Radial Velocity Constraint}} + \alpha^2 \underbrace{(U_x^2 + U_y^2 + U_z^2 + V_x^2 + V_y^2 + V_z^2 + W_x^2 + W_y^2 + W_z^2)}_{\text{Velocity Smoothness Constraint}} + \beta^2 \underbrace{((U - U_{I_s})^2 + (V - V_{I_s})^2 + (W - W_{I_s})^2)}_{\text{Least Squares Velocity Consistency Constraint}} + \sum_{i=1}^n \gamma_i^2 \underbrace{((U - U_{wpr_i})^2 + (V - V_{wpr_i})^2 + (W - W_{wpr_i})^2)}_{\text{Windprofiler Velocity Consistency Constraint}} \right) dX dY dZ, \quad (3)$$

where the γ_i s are the Lagrange multipliers for the fourth constraint. The value of γ_i at each voxel is cal-

culated from a 3D Gaussian function based on the distance between it and the location of the i^{th} point of the Windprofiler radar:

$$\gamma_i = \frac{\Gamma}{(2\pi)^{\frac{3}{2}} \prod_{k=1}^3 \sigma_k} e^{-\left(\frac{(x-x_{wpr_i})^2}{2\sigma_1^2} + \frac{(y-y_{wpr_i})^2}{2\sigma_2^2} + \frac{(z-z_{wpr_i})^2}{2\sigma_3^2}\right)}. \quad (4)$$

$\sigma_1, \sigma_2, \sigma_3$ are the three standard deviations that specify the shape of the 3D Gaussian distribution according to the distance between the points where \vec{V} and \vec{V}_{wpr_i} are measured in each of the 3 dimensions, while $\Gamma = 1000$ is a preset constant value. For our experiments, σ_1 and σ_2 have the value 20.0, reflecting the large x and y range of values, while $\sigma_3 = 0.4$, reflecting the much smaller range in the z values. The “goodness” of these parameter values are confirmed by synthetic and real data experiments.

We use Gauss-Seidel iterations on the Euler-Lagrange equations derived from Equation (3) to compute the flow. At the start of the calculation, \vec{V}^0 is set to zero. Until a specified number of iterations (150) or while the difference between the k^{th} and $(k+1)^{th}$ velocity fields remains greater than a threshold $\tau = 10^{-3}$, the iterative calculation continues. At the end, the velocity field is set to the last iteration’s velocity field. We refer to this as the **refined** optical flow while the original optical flow without the Windprofiler constraint is referred to as the **unrefined** optical flow (Barron et al., 2005).

2.1 Synthetic Data Generation

The synthetic data is determined by two factors: the constant **base velocity** and the changeable **variation velocity**:

$$\vec{V} = \vec{V}_{base} + \vec{V}_{var}. \quad (5)$$

Vector $\vec{V}_{base} = (U_{base}, V_{base}, W_{base})$ is a constant (base) vector, independent of 3D location. Vector \vec{V}_{var} is given as:

$$\vec{V}_{var} = \frac{K}{10.0} \vec{V}_{base} \cdot (\sin(x - \omega_x), \sin(y - \omega_y), \sin(z - \omega_z)). \quad (6)$$

The three phase parameters $\omega_x, \omega_y,$ and ω_z shift the overall distribution of full velocity to different positions. The variation level K determines the highest possible portion of variation that can be added, while the specific portion added at point \vec{p} is decided by its position. Note that $K = 0$ will not generate any variation. As K increases from 0 to 5, the possible maximum value of variation will change from 0% to 50% of the base velocity \vec{V}_{base} .

For the purpose of simulating noise added to raw data during the radar detection procedure and evaluating our algorithm’s robustness to noise, we also add

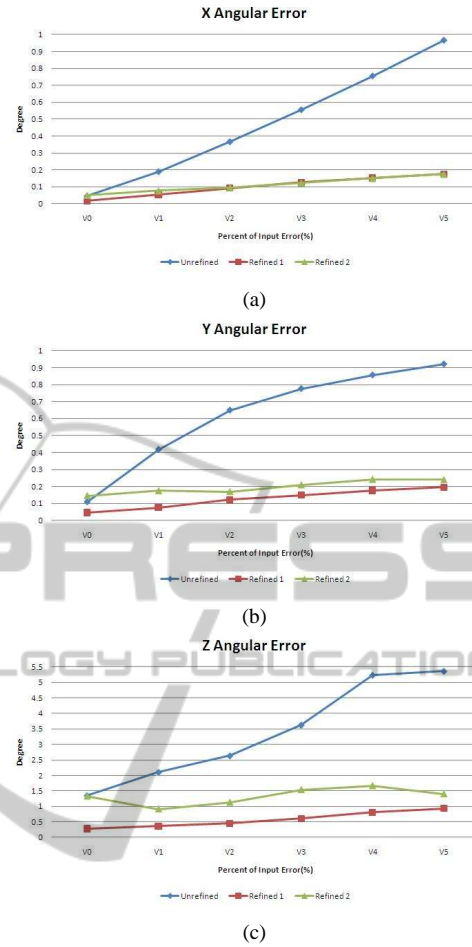


Figure 3: Error results of the synthetic data for all K values: (d) the average x angular error, (e) the average y angular error and (f) the average z angular error. Refine1 (red) lines represent 0% Windprofiler error while Refine2 (green) lines represent 10% Windprofiler error.

various percentages of Gaussian noise ($N[0,1]$) to the synthetic radial velocity data.

2.2 Error Metrics

The quantitative analysis includes the overall output error, E_O , and for each voxel, i , the magnitude error, E_{M_i} , the direction error, E_{D_i} , and the component angular errors, $E_{A_{x_i}}, E_{A_{y_i}}$ and $E_{A_{z_i}}$. These error metrics are defined as:

$$E_O = \frac{\|\vec{V}_e - \vec{V}_c\|_2}{\|\vec{V}_c\|_2} \times 100\%, \quad (7)$$

$$E_{M_i} = \frac{|\|\vec{V}_{e_i}\|_2 - \|\vec{V}_{c_i}\|_2|}{\|\vec{V}_{c_i}\|_2} \times 100\%, \quad (8)$$

$$E_{D_i} = \arccos\left(\frac{\vec{V}_{e_i} \cdot \vec{V}_{c_i}}{\|\vec{V}_{e_i}\|_2 \|\vec{V}_{c_i}\|_2}\right) \times \frac{180^\circ}{\pi}, \quad (9)$$

$$E_{A_{x_i}} = \arccos(\hat{V}'_{c_{x_i}} \cdot \hat{V}'_{e_{x_i}}), \quad (10)$$

$$E_{A_{y_i}} = \arccos(\hat{V}'_{c_{y_i}} \cdot \hat{V}'_{e_{y_i}}), \quad (11)$$

$$E_{A_{z_i}} = \arccos(\hat{V}'_{c_{z_i}} \cdot \hat{V}'_{e_{z_i}}), \quad (12)$$

where \vec{V}_{e_i} is the retrieved velocity at location i and \vec{V}_{c_i} is the correct velocity at location i used by the synthetic data generation. Given estimated velocity $\vec{V}_e = (V_{e_x}, V_{e_y}, V_{e_z})$ and correct velocity $\vec{V}_c = (V_{c_x}, V_{c_y}, V_{c_z})$, the component angular error calculation in Equation (10), for example, uses $\vec{V}'_{e_x} = (V_{e_x}, 1)$ and $\vec{V}'_{c_x} = (V_{c_x}, 1)$. Note that we use \hat{V} to indicate that \vec{V} has been normalized. The component angular errors provide a single numerical value that captures both magnitude and angular error and avoids the zero division problem inherent in relative error metrics (Barron et al., 1994). To summarize the algorithm's performance as a whole, we present the averaged metrics below.

3 EXPERIMENTAL RESULTS

Figure 1 shows the unrefined and refined optical flow for our synthetic data. The blue circle center indicates the position of the Harrow Windprofiler in the real data (and we use the same position in the synthetic data) while its radius is $2\sigma_x$ (95% confidence). Note that the velocity in the undefined case is to the right and downwards while the velocity in the refined case is also to the right but less downwards. Figs. 2 and 3 shows the various averaged error measures inside the Windprofiler 95% confidence circle for the unrefined (blue) and refined flow for 20% Doppler data noise and 0% (red) and 10% (green) Windprofiler noise. Obviously, the Windprofiler data greatly improves the flow computation.

We present some preliminary results for our measured Doppler and Windprofiler data. Figs. 4a and 4b show the unrefined and refined UV optical flow fields for the Detroit Doppler data at 12:35:10 of August 19th, 2007. We also show the W component of optical flow along the z (height) axis in Figs. 5a and 5b. Component velocities in these figures are shown as coloured pixels. They correspond to the standard numerical values used for NEXRADII data. Note that these component colours have replaced the radial velocity magnitude colours in Figs. 4a and 4b.

It is clear from the z component flow field images that the refined method significantly changes the flow field around the Windprofiler radar. Figure 4a has the unrefined flow going north while Figure 5a has the refined flow going south. We see a significantly improved recovery of component velocity W in the z direction. In the unrefined component flow shown in

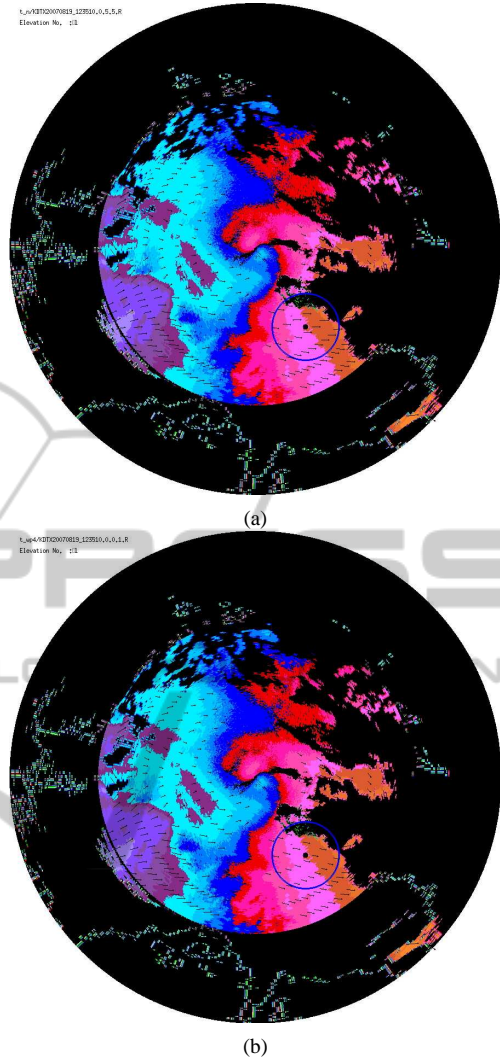


Figure 4: Full velocity retrieved from the Detroit Doppler (and the Harrow Windprofiler) data on August 19th, 2007 at 12:35:10: (a) the unrefined UV optical flow and (b) the refined UV optical flow. The blue circle indicates the location of the Windprofiler radar.

Figure 5a, there is a large area where the component velocities are the maximum possible value (yellow). However, in the component flow shown in Figure 5b, it is obvious that a more reasonable result has been obtained in the area surrounding the Windprofiler radar. We observe a strong upward velocity component in the areas not overlapped by the Windprofiler radar but a significant downward velocity component in outer area around the Windprofiler radar. This is due to the fact that the Windprofiler constraint adopted different velocity values for the Doppler voxels according to their actual distances from the Doppler radar points.

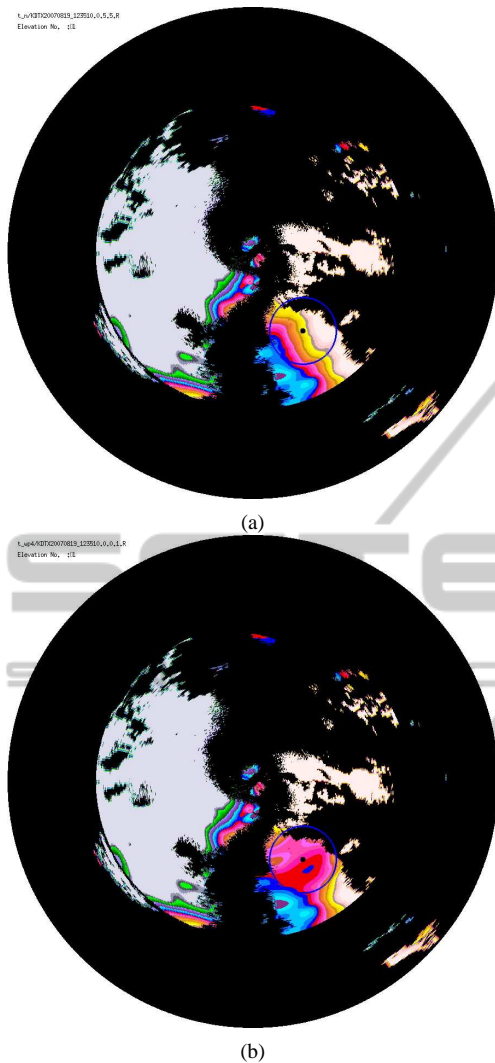


Figure 5: Full velocity retrieved from the Detroit Doppler (and the Harrow Windprofiler) data on August 19th, 2007 at 12:35:10: (a) the W component of the unrefined optical flow and (b) the W component of the refined optical flow. Again, the blue circle indicates the location of the Windprofiler radar.

4 CONCLUSIONS

In this paper we briefly described combining Windprofiler data at the Harrow radar station with NEXRADII Doppler data from Detroit to produce an arguably more accurate optical flow field in the vicinity of the Windprofiler radar. We showed that qualitatively, more accurate and detailed information could be recovered along the z (height) dimension and sometimes in the x and y dimensions. However, it is noted that a Windprofiler radar only covers a small area compared to a Doppler radar. This limits its ap-

plication. Our framework can handle more Windprofiler and Doppler radars but we do not yet have results for more than one Windprofiler radar data set and one Doppler radar data set that overlap. We have recently shown that more accurate optical flow can be recovered in the overlapping (oval) areas of 2 Doppler radars (Y. Zhang and Mercer, 2010) using our regularization framework. Using multiple Doppler and Windprofiler radars to track storms over long periods of time is a current area of research.

ACKNOWLEDGEMENTS

We acknowledge funding from the Natural Sciences and Engineering Research Council of Canada, and the Canadian Foundation for Innovation.

REFERENCES

- Barron, J., Fleet, D., and Beauchemin, S. (1994). Performance of optical flow techniques. *Int. Journal of Computer Vision*, 12:43–77.
- Barron, J., R.E.Mercer, Chen, X., and Joe, P. (2005). 3d velocity from 3d doppler radial velocity. *Intl. Journal of Imaging Systems and Technology*, 15:189–198.
- Easterbrook, C. C. (1975). Estimating horizontal wind fields by two-dimensional curve fitting of single doppler radar measurements. In *16th Radar Meteorology Conf.*, pages 214–219.
- Horn, B. K. P. and Schunck, B. G. (1981). Determining optical flow. *Artificial Intelligence*, 17:185–204.
- Lhermitte, R. M. and Atlas, D. (1961). Precipitation motion by pulse doppler. In *9th Weather Radar Conference*, pages 218–223.
- Lucas, B. D. and Kanade, T. (1981). An iterative image-registration technique with an application to stereo vision. In *DARPA Image Understanding Workshop*, pages 121–130.
- Waldteufel, P. and Corbin, H. (1979). On the analysis of single-doppler radar data. *J. of Applied Met.*, 18:532–542.
- Y. Zhang, J. B. and Mercer, R. E. (2010). 3d optical flow from single and dual doppler radars. In *Irish Machine Vision and Image Processing Conference (IMVIP2010)*.